DOI: 10.1002/ ((please add manuscript number))

Article type: Full Paper

Cloaking Dynamics on Lubricant-Infused Surfaces

A. Alperen Günay, Soumyadip Sett, Qiaoyu Ge, TieJun Zhang, Nenad Miljkovic**

Dr. A.A. Günay, Dr. S. Sett

Department of Mechanical Science and Engineering, University of Illinois at Urbana–Champaign, Urbana, IL, 61801, USA

Prof. N. Miljkovic

Department of Mechanical Science and Engineering, University of Illinois at Urbana–Champaign, Urbana, IL, 61801, USA

Department of Electrical and Computer Engineering, University of Illinois at Urbana – Champaign, Urbana, IL, 61801, USA

International Institute for Carbon Neutral Energy Research (WPI-I2CNER), Kyushu University, 744 Moto-oka, Nishi-ku, Fukuoka, 819-0395, JAPAN

Materials Research Laboratory, University of Illinois at Urbana–Champaign, Urbana, IL, 61801, USA

Q. Ge, Prof. T.J. Zhang

Department of Mechanical Engineering, Masdar Institute, Khalifa University of Science and Technology, Abu Dhabi, UAE

Email: nmiljkov@illinois.edu, gunay@photon.t.u-tokyo.ac.jp

Keywords: Evaporation, Lubricant, LIS, Cloaking, Coalescence

Lubricant-Infused Surfaces (SLIPSs/LISs) enable omniphobicity by reducing pinning due to creation of an atomically smooth liquid-liquid interface. Although SLIPSs/LISs provide efficient omniphobicity, the need for lubricant adds additional barriers to heat and mass transport and affects three-phase contact line dynamics. Here, evaporation dynamics of microscale water droplets on SLIPSs/LISs were investigated using steady and transient methods. Although steady results demonstrate that evaporation on SLIPSs/LISs is identical to solid functional surfaces having equivalent apparent contact angle, transient measurements show significant increases in evaporation timescale. To understand the inconsistency, high-speed optical imaging was used to study the evaporating droplet free interface. Focal plane shift imaging enabled the study of cloaking dynamics by tracking satellite microdroplet motion on the cloaked oil layer to characterize critical timescales. By decoupling the effect of substrate material and working fluid via experiments on both microstructured copper oxide and nanostructured boehmite with water and ethanol, it is demonstrated that lubricant cloaking cannot be predicted purely by thermodynamic considerations. Rather, coalescence dynamics, droplet formation, and surface interactions play an important role on establishing cloaking. The outcomes of this work sheds light onto the physics of lubricant cloaking, and provide a powerful experimental platform to characterize droplet interfacial phenomena.

1. Introduction

Phase change heat transfer plays a vital role in thermal engineering processes such as consumer electronics cooling[1], power generation[2], and thermal management[3] due to the high latent-to-specific heat of most liquids[4]. Condensation[5], boiling[6] and evaporation[7] have been studied extensively in the past. With recent advancements in nanomanufacturing, surface structuring for enhanced phase change has gained much interest[5b, 8]. Such tailored surfaces can lead to unique wettability including superhydrophobic[5b, 9] and biphilic[8b, 10] states, which have been shown to enhance condensation[11]. However, water-repellent structured surfaces perform poorly with low surface tension fluids such as alcohols and hydrocarbons due to the non-polarity of these fluids[12]. Recently, omniphobic slippery liquid-infused porous surfaces (SLIPSs) or lubricant-infused surfaces (LISs) have been developed. These surfaces utilize an atomically smooth liquid-liquid interface to ensure chemical and topographical homogeneity, and hence droplet pinning reduction[13]. The surfaces are prepared by infusing a structured superhydrophobic surface with a low- surface energy lubricant[14], and have been shown to be highly promising for various applications including enhanced condensation[12, 13b], anti-icing[15], antifouling[16], self-healing[17], and in biomedical devices[18]. However, although having a smooth and slippery surface has many advantages[19], the lubricant layer adds an additional barrier to heat and mass transport from the substrate to the working fluid (evaporation), or vice-versa (condensation). Furthermore, the presence of the lubricant alters interfacial dynamics, affecting the three-phase contact line which governs phase-change[20]. Hence, evaporation and condensation dynamics on SLIPSs/LISs can differ from those observed on solid surfaces.

In this study, we employ our previously established steady droplet evaporation method to examine dynamics of water droplet evaporation on a variety of SLIPSs/LISs[7c]. We vary the characteristic droplet size ($75 \leq R \leq 375$ μm, where R is the droplet radius) at ambient conditions

(T_∞ = 25 $\pm$ 0.5°C, ϕ = 50% $\pm$ 5%, P = 101 kPa, where T_∞, ϕ, and P are the laboratory air temperature, relative humidity, and pressure, respectively) to investigate effects of non-dimensional parameters such as Bond, Capillary, Rayleigh, and Ohnesorge numbers on droplet evaporation dynamics. Our results show that droplet evaporation rates on SLIPSs/LISs are comparable to solid functional surfaces having equivalent apparent contact angles. However, traditional transient evaporation rate measurements reveal anomalously higher evaporation timescales for droplets on fluorinated-oil LISs. To characterize the underlying physics governing this evaporation timescale discrepancy, we use high-speed focal plane shift imaging to optically investigate dispensed microdroplet mobility on the free interface of the evaporating droplet. Our results clearly demonstrate the presence of an additional lubricant layer encapsulating the outer surface of the evaporating droplet, commonly termed as cloaking[13c, 21]. The cloaking layer is formed when a balance between the interfacial energies of the fluids cannot be formed, which leads to spontaneous spreading of the lubricant on the droplet interface[13b, 13c]. This cloaking layer acts as an additional barrier to heat and mass transport from the liquid-vapor interface. Cloaking is governed by the interfacial energies of the lubricant and the evaporating liquid, with the substrate surface playing no role in the process[13c]. We demonstrate that for cloaked water droplets, the addition of microdroplets to the larger droplet creates highly mobile satellite droplets. We utilized trajectory tracking to follow satellite droplets on the droplet free interface to help elucidate the physics governing cloaking. When the influx of microdroplets is arrested, a steady movement of existing satellite droplets towards the top of the evaporating droplet (against gravity) exists, demonstrating cloaked oil layer mobility. However, when the flow of microdroplets is continuous, we observe satellite droplet motion toward the evaporating droplet contact line due to impact-induced capillary waves. To test our hypotheses, we conducted further experiments with ethanol, demonstrating the importance of droplet history and dynamics, as opposed to simple thermodynamics of cloaking phenomena. The outcomes of this work sheds light onto the physics governing cloaking of lubricants and offer a powerful platform for studying interfacial cloaking phenomena on SLIPS/LIS.

2. Results and Discussion

2.1. Cloaking

The lubricant encapsulates or coats the outer surface of the evaporating droplet in a perfect wetting scenario when an equilibrium between the interfacial energies cannot be attained, which is termed as cloaking[22]. Cloaking takes place when the spreading coefficient of the lubricant (Equation 1) on the evaporating liquid is positive ($S_{\mathrm{ol}} > 0$), which dictates that the lubricant will spontaneously encapsulate the droplet. The spreading coefficient S_{ol} is given by:

$$S_{\mathrm{ol}} = \gamma_{\mathrm{l}} - \gamma_{\mathrm{o}} - \gamma_{\mathrm{ol}}\,, \tag{1}$$

where γ_{o} and γ_{l} are the liquid-vapor surface tensions of the lubricant (or oil) and the working fluid, respectively, and γ_{ol} is the interfacial tension between the lubricant and the working fluid. Although the liquid-vapor surface tensions of both the lubricants and working fluids are intrinsic liquid properties and readily available in literature (**Table 1**), the interfacial tensions between the working fluids and the lubricants need to be calculated. They can be determined either theoretically using statistical thermodynamic models such as Fowkes method[23] or van Oss, Chaudhury and Good (vOCG)[23b, 24] method, or experimentally measured using rheometers, tensiometers or pendant drop method[14, 19, 25]. Previous studies have shown that for non-polar lubricants such as the ones used here (with the exception of ionic liquid BMIm), the theoretical calculations and experimental measurement of interfacial tensions yield similar results[14, 19]. For the vOCG method, the interfacial tension can be expressed as a combination of the non-polar Lifshitz - van der Waals (LW) interactions and polar Lewis acid-base (AB) components (Equation 2). For non-polar molecules, the Lewis acid-base components are negligible since these materials do not exhibit electron acceptor nor electron donor properties, leaving only Lifshitz - van der Waals interactions as the only contributing term to their overall liquid-vapor surface tension. Moreover, both components of surface tensions for regular solvents are readily found in literature[23b, 26], utilizing which the interfacial tension between the working fluid and non-polar lubricant can be calculated as:

$$\gamma_{ol} = \gamma_o + \gamma_l - 2(\gamma_o{}^{LW}\gamma_l{}^{LW})^{0.5}, \quad (2)$$

where the superscript LW represents the Lifshitz – van der Waals component. The results of the interfacial tension and spreading coefficient analysis for the used lubricants and working fluids are summarized in **Table 2**. Note that all tested lubricants in this study, except ionic liquid BMIm, are non-polar, and hence their interfacial tensions with the working fluids can be calculated using Equation 2. However, BMIm being polar in nature, the individual surface tension components were not available. Ionic liquid BMIm is partially soluble in water, and can result in decrease of the intrinsic liquid surface tension from 72.7 mN m^{-1} (pure water) to 42 mN m^{-1} (well-mixed ionic liquid-water solution)[13b]. However, we recently showed that such equilibrium ionic liquid-water mixture is not the scenario during phase change operations (condensation, evaporation), and the working fluid surface tension should be taken that of pure water[25]. The positive spreading coefficients calculated (Table 2) for the Krytox lubricants for water indicates that irrespective of the oil viscosity, these lubricants will cloak water droplets. Interestingly, though the Fomblin oil is very similar to the Krytox oils in terms of chemical structure and viscosity, its slightly higher surface tension makes the spreading coefficient marginally negative. It is worth noting though, given the calculations were done considering fixed surface tension values neglecting the effect of temperature, very small values of spreading coefficients ($|S| < 2$) are not a definite indication of whether the lubricant will cloak the working fluid. Carnation oil on the other hand has a significantly negative spreading coefficient, and can be expected to not cloak water droplets. For ionic liquid BMIm, considering its partial solubility in water leads to negative spreading coefficient (non-cloaking)[13b], whereas considering the droplet to be that of pure water leads to positive spreading coefficient (cloaking)[25], as listed in Table 2.

2.2. Droplet Evaporation

Lubricant infused surfaces differ from solid surfaces due to the lubricant separating the droplet from the solid substrate, which induces additional substrate-to-droplet thermal resistance, $R_{th,base,NS}/R_{th,base,LIS} \approx 0.7$, where NS and LIS represent nanostructured surface and lubricant infused surface,

respectively. For details of the thermal resistance analysis, see Section S1 of the Supporting Information. Furthermore, the ability of the lubricant to cloak and encapsulate droplets with a micro/nanoscale thick lubricant layer presents the opportunity to create an additional resistance to mass transfer at the liquid-vapor interface, $R_{\mathrm{diff,int,NC}}/R_{\mathrm{diff,int,C}} \ll 1$, for a cloaking layer thickness of 1 μm, where the subscript diff represents diffusion (mass transfer), and NC and C represent non-cloaking and cloaking, respectively. Although both thermal resistances contribute to lower heat transfer, a simple thermal resistance analysis for a cloaked droplet dispensed on a structured surface (CuO or boehmite) reveals that $R_{\mathrm{th,base}}/R_{\mathrm{th,int,C}} \ll 1$ for a cloaking layer thickness of 1 μm (Section S1, Supporting Information). Therefore, the presence of any encapsulating lubricant layer decreases the evaporation rate compared to non-cloaked droplets. To test our hypothesis, we studied hydrophobic-state droplets to ensure that evaporation is governed by the liquid-vapor interface[7c] and contact line region instead of droplet or substrate conduction. Furthermore, the presence of non-condensable gases at the liquid-vapor interface ensures that diffusional mass transfer effects at the liquid-vapor interface govern evaporation[7c]. **Figure 1** shows the water droplet evaporation rate ($\dot{m}$) as a function of droplet radius (R) on a variety of different LISs as well as the solid hydrophobic control sample (Si-HTMS). Accordingly, LISs having similar apparent advancing contact angle and droplet radii as that of the control display lower evaporation rates due to the added diffusional resistance. Similar evaporation rates were observed on LISs impregnated with Krytox and Fomblin fluorinated oils, regardless of their difference in viscosity, surface tension, and other physical properties. Furthermore, different rates of evaporation were observed between the fluorinated oils and the carnation oil LISs. Conclusions of higher evaporation rate due to the non-cloaking nature of Carnation oil could not be drawn since the apparent advancing and receding contact angles are different for carnation oil and the fluorinated oils (**Table 6**).

To verify if cloaking affected droplet evaporation mass transfer, we conducted experiments using the traditional transient-based evaporation technique on the same samples[27]. We deposited water droplets of identical size and allowed them to evaporate completely, measuring the droplet

radius as a function of time. Furthermore, we measured the total time for complete droplet evaporation (t_e). Results of the transient method displayed a significant difference from the steady method. **Figure 2** shows t_e as a function of initial droplet radius (R_i) on the different LISs. It took significantly less time for droplets to evaporate on the solid hydrophobic control sample (Si-HTMS) and the Carnation oil LIS than on the fluorinated oil LISs. The lower t_e for Si-HTMS with the transient method is in accordance with the higher evaporation rate measured with the steady method (Figure 1). Given that we maintained similar starting droplet radii for evaporation using the transient method, the Carnation oil LIS had a smaller volume of water for an equivalent R_i when compared to the rest of the tested samples due to its lower apparent advancing contact angle (Table 6), yielding lower t_e. Figure 2 shows that K1525 and F25/6 surfaces displayed identical evaporation behavior, as expected given their similar thermophysical properties (Table 1). The K16256 displayed longer t_e than the rest of the samples due to different cloaking physics induced by different thermophysical properties of the lubricant (Table 1). We hypothesize that the difference in the evaporation rates (Figure 1) and total evaporation times (Figure 2) is attributed to the different viscosities of the lubricants (Table 1). According to the Stokes – Einstein equation, mass diffusivity (D) and dynamic viscosity (μ_0) are inversely related ($D \sim 1/\mu_0$).[28] Therefore, the diffusivity is 90% lower in K16256 when compared to the other tested lubricants due to its 10X higher dynamic viscosity. Hence, water molecules diffusing through the lubricant layer at the liquid vapor interface encounter a higher mass transfer resistance for higher viscosity lubricant (K16256).

The presence of cloaking implies an additional lubricant layer covering the outer surface of the water droplet. The cloaking in turn affects the permeation of dispensed microdroplets for the steady experiments (Figure 1) into the larger evaporating droplet, which introduces uncertainty in the measured evaporation rate due to the smaller droplets evaporating while coalescing with the larger evaporating droplet. To shed light on the physics dominating the microdroplet addition process, and to experimentally confirm the presence of cloaking, we developed an experimental

platform to study the droplet free interface, and used it to evaluate the relevant time scales and properties governing cloaking.

2.3. Focal Plane Shift Imaging

For the steady state evaporation experiments using the microgoniometer, the microdroplets are dispensed form the piezoelectric dispenser at a frequency of 40-80 Hz, making it difficult to optically resolve microdroplets impacting the larger droplet using the regular microgoniometer camera setup (200 fps limit). To experimentally visualize cloaking, we developed a different imaging technique, which allowed us to monitor dispensed microdroplet mobility as it approaches the free interface of the larger droplet residing on the surface. We interfaced a high-speed camera (Phantom v711) with 20X-100X magnification lens to observe microdroplet addition onto larger evaporating droplets. We first bring the droplet to a steady state size and focus the camera to obtain a sharp image of the droplet contour. Then, we slightly shift the focal plane (~10 μm), enabling us to visualize the oil layer outside of the evaporating droplet (**Figure S2, Video S1**). By capturing videos at high speed (5,000-10,000 fps), we can directly observe the satellite droplets on the cloaked lubricant layer enabling us to study the lubricant motion on the droplet when the monodisperse droplet flow is turned off. Satellite droplets that are formed on the lubricant layer are tracked to determine whether there is lubricant motion on the droplet to check for the presence of cloaking. To ensure that the observed motion of dispensed microdroplets does not occur due to air-film drainage and coalescence physics[29], we first conducted experiments on the control sample (Si-HTMS) and demonstrated that droplets approaching the liquid-vapor interface coalesce upon interaction and do not behave like those observed on LISs (**Video S9**). Representative time-lapse images of the tracked microdroplets when droplet deposition is turned off are shown in **Figure S3** of the Supporting Information (**Video S2**).

To verify that the presence of cloaked layer is not an optical effect, the imaging technique was applied to an evaporating steady droplet when the flow of monodisperse droplets from the

piezoelectric dispenser was on. For the studied LISs, mobility of the dispensed monodisperse droplets were captured (**Figure 3, Video S3**). We distinctly see the microdroplet deposit on the lubricant layer and move along the free interface before coalescing with the larger evaporating droplet. In the absence of the cloaked layer, a microdroplet coming in contact with a larger droplet of the same fluid (water in this case) instantaneously coalesces[29] (Video S9).

The results of the image analysis for cloaking show that the fluorinated Krytox oils for all viscosities cloak water droplets as predicted by the thermodynamic analysis (Table 2). Furthermore, F25/6 lubricant, which was predicted to not cloak water droplets, was in fact observed to cloak water droplets. However, as mentioned before, the calculated spreading coefficient of F25/6 was very close to zero (≈0.1 mN m^{-1}); indicating uncertainty with regards to cloaking prediction. To observe cloaking phenomena, we also studied ionic liquid BMIm LIS. Due to the hydrophilicity of water droplets on BMIm LIS, we did not study steady-state evaporation as no control surface was available to benchmark evaporation rates. Interestingly, in contrast to previous observations where BMIm did not cloak water condensate droplets during water vapor condensation[13b], we observed BMIm to cloak water droplets. As mentioned earlier, due to partial solubility of BMIm in water, surface tension of the well-mixed BMIm-water reduces to 42 mN m^{-1} at equilibrium, resulting in a negative spreading coefficient of -4.8.[13b] However, we distinctly observe secondary microdroplets on the larger evaporating droplet, clearly indicating the presence of an additional oil layer between the two droplets (**Figure 4**, **Video S4**). The observation is in agreement with our recent work which showed for ionic liquid BMIm LIS, cloaking of water droplets occurs during condensation[25]. The time scale of dissolution of ionic liquid in water is much slower as compared to the encapsulation of the water droplet by the lubricant, leading to formation of the cloaked layer. Additionally, by considering the polar and non-polar components of the surface tension of the ionic liquid (i.e. no dissolution of ionic liquid), the spreading coefficient of BMIm with water does indeed turn out to be positive, indicating cloaking is favorable[14].

Though the microdroplet mobility on the cloaked layer helps us to calculate the velocities and timescales of cloaking experimentally, more in-depth analysis of the physics governing cloaking at a fundamental level is needed.

2.4. Cloaking Timescales

From the time lapse images (Figure 3 and 4), it is evident that cloaking in the steady evaporation process is governed by three different time scales: 1) time for the lubricant to completely encapsulate the evaporating droplet on the surface, 2) time for the lubricant layer between the monodisperse droplet and the larger evaporating droplet to drain and allow coalescence, and 3) time for the lubricant to re-cloak the coalescing region. To understand the physics governing the cloaking process, we decoupled the three processes and studied them separately.

The first important time scale is the time taken for the lubricant infused within the surface structures to cloak or encapsulate the entire surface of the evaporating droplet. In the decoupled time scale estimate, we assume the impacting monodisperse droplet to have negligible disturbance on the cloaked oil layer. We consider the location of the spreading along the radial front of the lubricant from the substrate surface to the droplet[22, 30]. The spreading of lubricant on a droplet consists of two different stages; formation of a monolayer driven by a balance between the shear stress at the lubricant-water interface and surface tension gradient, followed by the formation of a nanofilm[30]. For the monolayer, the radial front location of the cloak is:[31]

$$R_{\mathrm{s,m}} = \sqrt{\frac{4S_{\mathrm{ol}}}{3\sqrt{\mu_0\rho_0}}}\,{t_{\mathrm{s,m}}}^{3/4}\,, \tag{3}$$

where μ_0 and ρ_0 denotes the dynamic viscosity and density of the lubricant, respectively. For the nanofilm regime, three contributions affect the flow: inertial, viscous, and capillary forces. In order to decouple the relative importance of these contributions, we calculate the Ohnesorge number[32] as $\mathrm{Oh} = \mu_0/(\rho_0 R\gamma_{\mathrm{o}})^{1/2}$.

For the water droplets residing on hydrophobic surfaces in this study, $\mathrm{Oh} > 1$, implying the flow to be viscous driven (**Table 3**). However, for ionic liquid BMIm, $\mathrm{Oh} < 1$, indicating inertia-driven flow. For viscous and inertia driven nanofilm flow, the relevant timescales are[22]:

$$\tau_{\mathrm{vis}} = \frac{\mu_0 R}{\gamma_{\mathrm{o}}}, \quad (\mathrm{Oh} > 1) \tag{4a}$$

$$\tau_{\mathrm{in}} = \sqrt{\frac{\rho R^3}{\gamma_{\mathrm{o}}}}, \quad (\mathrm{Oh} < 1) \tag{4b}$$

and the resultant spreading radial front location is:

$$R_{\mathrm{s,n}} = 0.87R\left(\frac{t_{\mathrm{s,n}}}{\tau_{\mathrm{vis}}}\right)^{0.3}, \quad (\mathrm{Oh} > 1) \tag{5a}$$

$$R_{\mathrm{s,n}} = 1.1R\left(\frac{t_{\mathrm{s,n}}}{\tau_{\mathrm{in}}}\right)^{0.45}. \quad (\mathrm{Oh} < 1) \tag{5b}$$

Assuming $R_{\mathrm{s,m}} = R_{\mathrm{s,n}} = R$ (Equation 5a and 5b), the radius of the droplet residing on the LIS, we can calculate $t_{\mathrm{s,m}}$ and $t_{\mathrm{s,n}}$ to provide us with an estimate of the total time it would take for the lubricant to cloak the droplet. Table 3 summarizes the results, indicating that $t_{\mathrm{s,m}} \sim t_{\mathrm{s,n}} \sim$ 1-10 ms. LIS K16256 exhibits the longest timescales, comparable to the time scale of dispensed microdroplets ($\sim 1/f$) due to its high viscosity. As the calculated cloaking time scales are smaller for all other lubricants than the dispensing time for the monolayer, we can safely assume that the water droplet is completely cloaked at the beginning of the steady evaporation process.

Having calculated the radial front location, we can now calculate the spreading velocity of the cloaking layer. For the monolayer, differentiating Equation 3 with respect to time gives:

$$U_{\mathrm{s,m}} = \sqrt{\frac{3S_{\mathrm{ol}}}{4\sqrt{\mu_0\rho_0}}}\, t_{s,m}{}^{-\frac{1}{4}}. \tag{6}$$

Similarly, for the nanofilm, differentiating Equation 5 yields:

$$U_{\mathrm{s,n}} = 0.26R\left(\frac{t_{\mathrm{s,n}}}{\tau_{\mathrm{vis}}}\right)^{0.3}\frac{1}{t_{\mathrm{s,n}}}, \quad (\mathrm{Oh} > 1) \tag{7a}$$

$$U_{\mathrm{s,n}} = 0.5R\left(\frac{t_{\mathrm{s,n}}}{\tau_{\mathrm{in}}}\right)^{0.45}\frac{1}{t_{\mathrm{s,n}}}. \quad (\mathrm{Oh} < 1) \tag{7b}$$

Assuming the monodisperse droplets impact the evaporating droplet in the vicinity of the spreading radial front (center), the created disturbance in the half circle is equal to the radius of the monodisperse droplet. Furthermore, assuming the impact does not affect the spreading velocity, we can calculate the timescale for the cloaking lubricant film to reform after being ruptured due to the coalescence between the droplets. Considering these velocities to be constant, we then divide them to the radius of the monodisperse droplet to find the relevant time for the oil to retravel to the center of the droplet. The obtained values are small (~0.1-1 ms) when compared to the time scale of the droplet dispensing (~10 ms) for our studied conditions (Table 3). Hence, the cloaking layer reforms almost instantaneously, and the evaporating droplet is fully cloaked when the subsequent monodisperse droplet hits the larger droplet residing on the LIS.

With the relevant time scales of cloak formation calculated, dynamics of the monodisperse droplet contact and coalescence with the larger droplet can be elucidated. Specifically, the time scale for the monodisperse droplet penetration of the oil layer due to the depletion of the cloaked lubricant between the two water droplets can be calculated. The presence of an oil layer between the two water droplets significantly delays coalescence[33]. Assuming a constant oil layer thickness and radius for a Newtonian fluid, we obtain the Navier - Stokes solution for drainage of the lubricant film between the two droplets by balancing the pressure due to curvature and viscous forces[33]:

$$\frac{\Delta P(t)}{R_{\mathrm{film}}} = \mu_0 \frac{\partial^2(u_r(z,t))}{\partial z^2}, \tag{8}$$

where $\Delta P(t)$ is the time-dependent pressure drop, R_{film} is the film radius, and $u_{\mathrm{r}}(z,t)$ is the radial drainage velocity. The analysis considers laminar, viscous dominated flow with the lubrication

approximation (only solving for radial drainage velocity $u_{\mathrm{r}}(z,t)$). Assuming a no slip boundary condition at the edges of the film, we obtain:

$$u_{\mathrm{r}}(z,t) = \frac{\Delta P(t)}{2a\mu_0}\left(z^2 - \left(\frac{H(t)}{2}\right)^2\right), \tag{9}$$

where H is the thickness of the oil layer and a is the oil layer radius. From here, we calculate the average velocity of the flow as:

$$u_{\mathrm{avg}} = -\frac{\pi\Delta P(t)\big(H(t)\big)^2}{6a\mu_0}. \tag{10}$$

To obtain an order of magnitude analysis at a given time, we assume that the oil layer thickness ($\sim 1-10$ μm)[25, 34], and monodisperse droplet radius (≈9 μm) are of the same order of magnitude, yielding:

$$u_{\mathrm{avg}} \sim \frac{a\Delta P}{\mu_0}. \tag{11}$$

Substituting the Laplace pressure for the top side of the meniscus ($D = 2R_{\mathrm{mono}}$) and the bottom side ($D = 2R$):

$$u_{avg} \sim \frac{a\gamma_{\mathrm{ol}}}{\mu_0}\left(\frac{1}{R_{\mathrm{mono}}} - \frac{1}{R}\right). \tag{12}$$

Finally, with the oil layer separating the water droplets having a radius a, $u_{\mathrm{avg}} \sim a/\tau_{\mathrm{depl}}$, where τ_{depl} is the time needed for the oil layer to be depleted. Substituting this into Equation 2, we obtain the time scale for the oil layer to be fully depleted for the two water droplets to come in contact:

$$\tau_{depl} \sim \frac{\mu_0}{\gamma_{\mathrm{ol}}}\left(\frac{1}{R_{\mathrm{mono}}} - \frac{1}{R}\right)^{-1}. \tag{13}$$

The depletion timescales ($\tau_{\mathrm{depl}} \sim 0.1$ ms) are much smaller than the time scales for droplet deposition ($t_{\mathrm{dep}} \sim 10$ ms) for all the studied LISs except for K16256 (Table 3). The obtained value for K16256 was $\tau_{\mathrm{depl}} \approx 9$ ms $\sim t_{\mathrm{dep}}$. The longer depletion timescales of K16256 helps explain the

observed enhanced mobility of monodisperse droplets on the outer shell of the evaporating droplet due to the non-depleted cloaking layer. These droplets cannot penetrate the lubricant cloaking layer fast enough to coalesce with the water droplet unlike the other LISs where depletion is faster, resulting in microdroplet evaporation prior to coalescence. Hence, only a portion of the incoming volume can coalesce with the large water droplet, leading to uncertainty in the steady evaporation measurements.

2.5. Impact of Monodisperse Droplet on the Evaporating Droplet

Monodisperse microdroplets supplied by the piezo dispenser and impacting the larger evaporating water droplet cloaked with a thin lubricant layer can create disturbances at the impacting interface (Figure 3, Video S3). In the absence of continuous flow from the dispenser, the movement of the cloaked oil layer drives the satellite water droplets against gravity (Video S2). However, given the presence of continually incoming fresh droplets, especially for K16256, which exhibits enhanced dispensed droplet mobility on the interface due to higher oil layer depletion time, we observed an interesting droplet behavior. Tracking analysis of individual microdroplets showed that the direction and speed of moving droplets change significantly in between adjacent microdroplet impacts. Towards the end of the cycle (*i.e.* right before impact of a fresh microdroplet), the satellite droplet in the cloaked layer moves in the upward direction (cloaking direction) against gravity towards the apex of the large evaporating drop with a negligible speed. However, as the fresh monodisperse droplet contacts the interface, the existing satellite droplet starts to move downward with a considerably higher speed until it equilibrates and starts to move upward again. Interestingly, the new satellite droplet moves downward at similar speeds, maintaining a uniform distance between the two satellite droplets and forming a train of droplets on the cloaking layer. This cycle is repeated until the monodisperse droplet evaporates or coalesces with the sessile droplet, and restarts with the arrival of a new monodisperse droplet (**Figure 5, Video S5**).

Although the satellite droplet sizes are considerably smaller than the evaporating droplet ($R_{\mathrm{mono}} \ll R$), the impacting droplets create capillary waves on the surface of the evaporating droplet. Such waves are not significant for non-cloaked droplets (*i.e.* water droplets on regular functional surfaces) due to immediate coalescence (Video S9). To estimate the expected velocities upon impact of microdroplets, we considered a uniform fluid (at rest) and solved the governing equations considering capillary wave phenomena. Due to the finite surface tension of the fluid in contact with air, the pressure discontinuity at the curved free surface is[35]:

$$[P]_{0^-}^{0^+} = \gamma_o \frac{\partial^2 \xi}{\partial x^2} \ , \tag{14}$$

where ξ represents the vertical displacement of the surface, and $\partial^2\xi/\partial x^2$ is the curvature of the surface. Hence, at the surface, the pressure boundary condition becomes:

$$\rho g \xi - P_1|_0 = \gamma_o \frac{\partial^2 \xi}{\partial x^2} . \tag{15}$$

Revisiting the Laplace equation with the velocity potentials ($\delta^2\phi/\delta x^2 + \delta^2\phi/\delta z^2 = 0$), and using it with Equation 14, the solution reduces to:

$$\left.\frac{\partial \phi}{\partial z}\right|_0 = \left.\frac{\gamma_o}{\rho g}\frac{\partial^3 \phi}{\partial x^2 \partial z}\right|_0 - \left.\frac{1}{g}\frac{\partial^2 \phi}{\partial t^2}\right|_0 . \tag{16}$$

The solution of Equation 16 yields:

$$\omega^2 = \left(gk + \frac{\gamma_o}{\rho}k^3\right)\tanh(kd) \ , \tag{17}$$

where ω is the frequency of the capillary wave, k is the wavenumber and d is the depth of the evaporating droplet ($d \approx 2R$). Considering the frequency of deposition is approximately equal to the frequency of the capillary wave, we can calculate the wavenumber ($k = \omega/c_{\mathrm{s}}$),[36] where c_{s} is the speed of sound in the lubricant. These values result in $kd \ll 1$; allowing us to approximate $\tanh(kd) \approx kd$; yielding:

$$\omega \approx k\sqrt{gd + \frac{\gamma_o}{\rho}k^2 d}\ . \tag{18}$$

where g is the gravitational acceleration. The phase velocity is defined as $v_{\mathrm{g}} = \omega/k$. Making use of the approximations and relative magnitudes of each terms, we obtain:

$$v_{\mathrm{g}} \approx \sqrt{gd}, \tag{19}$$

Table 4 summarizes the comparison between the calculated radial group velocities using Equation 19 and the values obtained from the focal-shift imaging experiments. The calculated values are always higher than the experimental values due to the non-stationary nature of the cloaked layer, where the oil moves in the opposite direction (*i.e.* in the direction to reform the cloak layer), hindering the motion of the satellite droplets. More importantly, the theoretical predictions and the experimental measurements are in the same order of magnitude, showing that droplet mobility on the interface is indeed caused by capillary waves induced on the evaporating droplet free surface by the impacting monodisperse droplet. A close investigation of the experimental results also displays that unlike other lubricants, the cloaking velocity of K1525 was larger than the radial component of the group velocity, causing the droplet to move against gravity on the outer surface of the droplet. Although we expect from our analyses that F25/6 and K1525 would exhibit similar behavior, we hypothesize that any observed differences stemmed from the quality of the K1525 sample.

To check that the upward motion is indeed solely due to cloaking (i.e. not due to internal effects), we study the Bond number ($\mathrm{Bo} = (\rho_{\mathrm{w}} - \rho_{\mathrm{v}})gL_{\mathrm{c}}^2/\sigma$, where ρ_{w} is the density of water, ρ_{v} is the density of vapor, $L_{\mathrm{c}} = V/A_{\mathrm{w}}$ is the characteristic length, and σ is the surface tension) and Marangoni number ($\mathrm{Ma} = L_{\mathrm{c}}\Delta T|\mathrm{d}\sigma/\mathrm{d}T|/\alpha\mu_{\mathrm{w}}$, where $|\mathrm{d}\sigma/\mathrm{d}T|$ is the derivative of the liquid-vapor surface tension (σ) with respect to temperature (T), α is the thermal diffusivity, and μ_{w} is the dynamic viscosity of water). Calculations yield $\mathrm{Bo} \ll 1$ (negligible buoyancy flows), and $100 < \mathrm{Ma} < 400$, on the order of the Marangoni number ($\mathrm{Ma}_{\mathrm{cr}}$ = 80 - 100)[37]. Previous studies show that for

sufficiently small droplets (R < 300 μm), Marangoni convection cannot initiate due to rolling caused by the instabilities of the mass center due to heating from below and cooling from above[38]. Since our studied droplets are smaller than 300 μm, we conclude that Marangoni effects are negligible here. We note that the calculated values provide an estimate of the key velocities and are used to primarily elucidate the physics. In reality, cloaking velocities depend on many factors such as the viscous drag between the satellite droplet and oil layer, and interference of capillary waves on impact.

2.6. Droplet Morphology Dependent Cloaking

Cloaking is governed by the interplay of the surface tensions of the lubricant and the working fluid (Equation 1). In principle, substrate surface structures should not influence cloaking dynamics. However, the surface may play a role when considering dynamics of cloak formation and access to free lubricant adjacent to the evaporating droplet. Smaller scale structures contain less lubricant as a reservoir for cloak formation and may play an important role. All aforementioned experiments were conducted on microstructured superhydrophobic CuO-based LISs. To confirm that the surface structures play no significant role in cloaking dynamics, we studied water droplet evaporation on boehmite-based LISs using the same lubricants outlined in Table 1. Due to the inherently different structure length scale of boehmite, the configuration of the lubricant infused in the microstructures is different[13c]. Briefly, the smaller length scale will result in increased solid surface area, effectively altering the interfacial force balance at the vapor-water-lubricant contact line. Thus, the apparent contact angles of water droplets (Table 6) on the boehmite LISs were different when compared to CuO-based LIS (**Table 5**). We investigated the satellite droplet velocities on K16256, SO-1000 and F25/6 to examine whether the different droplet shapes, with different apparent contact angles, influenced cloaking dynamics. These three lubricants were chosen for the boehmite LISs since they were the highest viscosity fluids of each group of lubricant. As hypothesized, the high-speed imaging revealed that the lubricants cloaked the water droplets on boehmite LISs in the same way as on

microstructured CuO LISs (Figure 5, Video S5). Our results show that satellite droplet velocities (both calculated and measured) decreased due to the decreasing apparent contact angles, which result in decreased radial group velocity components (Table 5). Therefore, the substrate plays a role in terms of droplet and interface geometry, and has no effect on cloaking behavior. The observed behavior is in agreement with the thermal resistance analysis (Section S1, Supporting Information). Although the thermal resistance to conduction from the base is much higher for CuO due to different nanostructure characteristic length scales ($l_{\mathrm{Al}}/l_{\mathrm{CuO}} \sim 0.1$, yielding $R_{\mathrm{th,base,Al}}/R_{\mathrm{th,base,CuO}} \approx 0.25$), the base resistance values are still much smaller than the interfacial resistance caused by cloaking ($R_{\mathrm{th,base,C}}/R_{\mathrm{th,int,C}} \ll 1$, Section S1, Supporting Information). Therefore, the substrate plays a negligible effect on the cloaking and evaporation dynamics for the range of structures studied here.

2.7. Hypothesis Testing: The Case of Ethanol Droplets

To test our formed hypothesis that the cloaking lubricant layer is governed by only the interfacial surface tensions, we studied droplet dynamics of evaporating ethanol droplets on CuO LISs using the focal shift imaging method. Specifically, we examined K1525, K1506, K16256, and F25/6, which do not cloak ethanol droplets[14, 19]. Based on the spreading coefficient values (Table 2), only the K1506 lubricant could possibly cloak ethanol droplets since it exhibits a slight positive spreading coefficient ($2 > S > 0$, Table 2). Interestingly, our experimental results showed that none of the studied LISs displayed cloaking with ethanol. Previous studies have also shown similar differences between the spreading coefficient calculations and experimental data, where the calculations predicted cloaking for ethanol droplets on K1506 ($S_{\mathrm{ol}} = 1.76$ mN m^{-1}) while the pendant drop method used to measure interfacial tension predicted otherwise ($S_{\mathrm{ol}} = -4.7$ mN m^{-1})[19]. The large difference exists because tabulated surface tension values used in the calculation are average values taken for ideal conditions neglecting temperature and humidity effects. Ideally, if surface tensions are measured using methods including a Wilhelmy plate, more accurate values can be obtained, leading to better agreement between theory (calculations) and experiments (pendant drop method).

2.8. Coalescence Dynamics of Cloaked and Non-Cloaked Droplets

Coalescence of similar sized cloaked droplets exhibit interesting physical behavior[33]. Coalescence is typically delayed due to the formation of a lubricant layer created by capillary forces as droplets approach one another[33]. The formation of the lubricant layer between coalescing droplets due to capillary forces may influence cloaking behavior of droplets due to the movement of the lubricant layer towards the interface for droplet sizes smaller than the capillary length ($\lambda_{\mathrm{C}} =$

$\sqrt{\gamma_{ol}/(\Delta\rho g)}$ ≈2.4 mm for the Krytox lubricant – water interface, ≈500 μm for the Krytox lubricant – ethanol interface)[39]. To study the effects of coalescence, we observed three different cases for similar sized water droplets: 1) $R = 115 \pm 5$ μm deposited on a CuO-based K1506 LIS (**Video S6**), 2) $R = 125 \pm 16$ μm deposited on a CuO-based K1525 LIS (**Figure 6, Video S7**), and 3) ethanol droplets of $R = 275 \pm 23$ μm deposited on a CuO-based K16256 LIS (**Figure S4, Video S8**). High-speed optical imaging revealed increased monodisperse water droplet mobility on the resulting sessile water droplet after coalescence. The results agree with our hypothesis that the capillary forces released during coalescence of two larger sessile droplets move the lubricant towards the apex of the droplet, creating a thicker layer on the top part of the resultant droplet interface. Furthermore, we observed that the non-cloaking ethanol droplet deposited on K16256 becomes cloaked after coalescence, possibly due to the formation of an oil layer on the free interface by capillary forces during coalescence. Hence, our observations imply that coalescence of droplets having similar size play an important role on cloaking behavior; which may result in pathways to achieve non-equilibrium states such as cloaking of initially non-cloaked droplets and increasing the thickness of the cloaking layer at the droplet apex. Due to the complexity of coalescence dynamics and lubricant cloaking, coupling of these two independent phenomena was beyond the scope of this work and is left for future studies.

Given the new understanding of cloaking dynamics, we can now begin to understand its importance on droplet evaporation (Figure 1 and 2). For our steady evaporation, the monodisperse microdroplet suffers from evaporation before it could coalesce with the larger evaporating droplet, leading to overestimated rates of evaporation for cloaking surfaces (Figure 1). The cloaking analysis revealed that viscosity of the lubricant and the interfacial tension between the lubricant and the working fluid govern delayed coalescence. However, for transient evaporation, it is evident that the presence of a cloaking layer on the interface significantly decelerates evaporation (Figure 2). The deceleration rate is governed by the viscosity of the lubricant due to its strong effect on mass diffusivity.

The current study sheds important light on LIS cloaking dynamics, which has major implications for designing stable robust LISs. For continuous and long-term operation, the primary issue with LISs is the loss of the infused lubricant. Though shear-induced lubricant drainage during droplet shedding might contribute significantly to oil depletion[40], cloaking remains one of the primary reasons for lubricant loss leading to LISs' failure[41]. Visualization techniques estimate the cloaking layer thickness to be of the order of ~1 μm[25], which for applications involving continuous droplet shedding such as phase change operations can lead to significant lubricant loss. For instance, LISs impregnated with Krytox oil initially showed dropwise condensation of toluene ($S_w > 0$) but within 1 hour of steady condensation the surface began to transition to filmwise mode[12a]. However, similar surfaces promote more than 7 hours of continuous dropwise condensation of ethanol and hexane ($S_w < 0$). Although different design criteria for LISs and SLIPSs[13c, 42] along with theoretical models calculating cloaking parameters predict effective lubricant-working fluid pairs[14, 19], rigorous analytical and visualization techniques are needed to provide sufficient evidence for durable and robust LISs.

Experimentally characterizing the cloaking layer has been a challenge for many researchers over the past decade. Methods such as ESEM[13b], optical microscopy[30], confocal fluorescence microscopy[13c, 34], CRYO-FIB/SEM[43], and interferometry[44] have been used to characterize the cloaking layer. Though some of these methods successfully visualized the lubricant layer beneath the droplet and at the contact line, they did not conclusively portray the layer of lubricant encapsulating the droplet. Our method allows the optical investigation of interface dynamics, and sets the foundation for enabling the characterization of cloaking.

Our results show that studying the thermodynamic phenomena in equilibrium alone cannot predict the cloaking dynamics accurately, since the droplet history and dynamics are as important as the thermodynamic phenomena in equilibrium for the formation of a cloak layer. We showed that coalescence of similar sized droplets leads to cloaking, *i.e.* lubricant loss on the surfaces. This poses a

problem on the durability of LIS since more lubricant would be lost as new droplets progressively shed and nucleate. Hence, thermodynamic theory alone should not be used for the design of LIS, and the outcomes of this work need to be carefully studied in order to increase durability.

Future studies should use the novel techniques developed on this manuscript to study other lubricant and fluid pairs in order to experimentally verify cloaking behavior and obtain a more detailed picture of cloaking dynamics. Recent works have demonstrated the role of the wetting ridge at the lubricant-droplet interface on the substrate playing a more significant role in lubricant drainage as compared to the cloaking layer[40a]. Condensate droplets shedding from horizontal LIS tubes break unequally, leaving behind satellite droplets on the tube surface, which was attributed to the wetting ridge. Yet, the lubricant cloaked the water droplet and decoupling of the shearing effect to the cloaking effect could not be determined experimentally. In this work, the different evaporation dynamics (Figure 1 and 2) point to the fact that though other effects exist, cloaking induced lubricant depletion cannot be neglected. It will be interesting in future to study droplet departure and lubricant depletion from LIS for non-cloaking lubricant-condensate pairs. Given LIS are widely used for condensation applications, the methods developed here can be implemented on actual condensing surfaces through nucleation of a condensed droplet, sequentially followed by injection of monodisperse droplets to investigate the cloaking behavior. Furthermore, the study could be extended to larger droplets (R > 1 mm) to investigate the coupled effects of capillary flows and internal flows (Marangoni and Buoyancy flow).

3. Conclusion

In this study, evaporation of water and ethanol droplets on LISs was investigated for a range of droplet size (75 to 375 μm). Our results demonstrate that for cloaked droplets, the steady-state method for evaporation characterization fails to capture actual evaporation dynamics due to the presence of an additional lubricant cloaking layer on the evaporating droplet. To study the lubricant layer cloaking the outer surface of the evaporating droplet, we developed a high-speed focal-shift

imaging technique and visually investigated the dynamics at the free droplet interface of the sessile evaporating droplet. We noticed secondary satellite droplets in motion within the cloaked oil layer of the evaporating droplet. Furthermore, we observed the presence of accumulation of the dispersed microdroplets on the outer interface of the sessile droplet due to the comparable time scales between lubricant layer depletion and droplet addition. Scaling analyses revealed that cloaking is governed by the reformation of the lubricant film after coalescence of two droplets, viscous effects, and droplet history and dynamics. To test our hypotheses, we varied the surface structure length scale and working fluid to determine their effects on cloaking dynamics. Our experiments showed that cloaking is governed by the interfacial tensions of the two fluids and that the surface structures play a limited role in the process. We observed that coalescence of similar sized sessile droplets alters cloaking behavior due to the movement of lubricant towards the interface caused by capillary forces formed during coalescence. Our work sheds light on the dynamics of cloaking on LISs and develops a powerful experimental platform to study cloaking phenomena of differing working fluids and LISs.

4. Experimental Section

Surface Fabrication and Characterization: Functionalized micro/nanostructured copper oxide (CuO) (from smooth copper, Cu) and boehmitized (Al(O)OH) aluminum (from smooth aluminum, Al) surfaces were impregnated with lubricant oil of various chemical structure and viscosity. The two different substrates were selected based on their differing structure length scales and hence lubricant capacity, with CuO microstructures approaching ~1 μm and boehmite nanostructures approaching ~100 nm. We used commercially available 2 x 2 cm flat Cu-110 (Part no. 8963K402, McMaster) and Al-6061 (Part no 89015K151, McMaster) tabs as the base metal surfaces for our experiments. Each metal tab was initially cleaned by dipping for 10 min each in acetone (CAS no. 67-64-1, Sigma-Aldrich), ethanol (CAS no. 64-17-5, Sigma-Aldrich), and isopropanol (CAS no. 67-63-0, Sigma-Aldrich), in succession, followed by rinsing with deionized (DI) water (CAS no. 7732-18-5,

Sigma-Aldrich). The Cu tabs were dipped into a 2 M hydrochloric acid (CAS no. 7647-01-0, Sigma-Aldrich) solution for 10 min to remove the native oxide layer on the surface, then rinsed multiple times with DI water and dried with clean nitrogen gas. Microstructured CuO surfaces were formed by immersing the cleaned Cu tabs into a hot (90 ± 3°C) alkaline bath of $NaClO_2$, NaOH, $Na_3PO_4{\cdot}12H_2O$, and DI water (3.75:5:10:100 wt%) for 10 min[45]. Nanostructured boehmite surfaces were formed by immersing the cleaned Al tabs into a boiling (≈ 100 ± 4°C) DI water bath for 60 min[46]. The structured CuO and boehmite surfaces were then functionalized by depositing heptadecafluorodecyltrimethoxy-silane (HTMS, CAS no. 83048-65-1, Gelest) by chemical vapor deposition. Briefly, samples were placed adjacent to a HTMS-toluene (CAS no. 108-88-3, Sigma-Aldrich) solution (5% v/v) in a sealed glass container inside an atmospheric pressure furnace (Blue M, Lindberg) at 80˚C for 3 hours[46a, 47]. For simplicity, we herein drop the delineation between SLIPS and LIS and call our samples LIS. The LIS samples were fabricated by dip coating the functionalized CuO and boehmite surfaces in the lubricant of choice (Table 1) for a total of 10 minutes. After dip-coating, the samples were removed and left standing in the vertical orientation in ambient laboratory conditions (≈24 ± 1°C) for approximately 24 hours to allow for gravitational drainage of excess lubricant[12b].

A range of lubricants were used in order to test how interfacial and thermophysical properties affect cloaking. Four different viscosity fluorinated oils: Krytox 1506, 1525 and 16256 (Chemours) and Fomblin Y25/6 (Solvay) were used. Furthermore, Carnation mineral oil (Sonneborn LLC), silicone oils having viscosities 5 cSt and 1000 cSt (Clearco Products), and ionic liquid 1-butyl-3-methylimidazoilium bis(trifluoromethylsulfonyl)-imide (BMIm, Sigma-Aldrich) were also studied. Both Cu and Al based LISs mainly displayed hydrophobic behavior as measured by the apparent advancing contact angle ($\theta_a \approx 115°$); however, surfaces impregnated with BMIm displayed hydrophilic behavior ($\theta_a \approx 65°$) due to the high liquid-vapor surface tension of BMIm ionic liquid. To provide a fair comparison with solid hydrophobic surfaces, a smooth silicon (Si) wafer functionalized

with HTMS ($\theta_a \approx 115°$) was used. The working fluids used were DI water and ethanol. Relevant properties of fluids used are shown in Table 1, with wetting properties summarized in Table 6.

Experimental Procedure: To study the evaporation dynamics of droplets on LIS, we used, microstructured superhydrophobic CuO infused with the lubricants outlined in Table 1. To compare the evaporation rates of droplets residing on LIS to solid functional surfaces having similar apparent advancing contact angle, we used a smooth Si wafer coated with HTMS (Si-HTMS, Table 6). BMIm ionic liquid and two different viscosity silicone oils, 5 cSt (SO-5) and 1000 cSt (SO-1000) were also used, however, are excluded from the evaporation analyses due to differences exhibited in apparent contact angle (BMIm, Table 6) when compared to the other LIS, and expected similar evaporation behavior to Carnation mineral oil (Silicone oils).

The steady state evaporation experimental procedure is described in detail in our previous work[7c]. Briefly, the setup consists of a high-speed camera (Phantom v711) integrated with a piezoelectric micro-goniometer (MCA-3, Kyowa Interface Science). The rate of microdroplet dispensing from the piezoelectric dispenser is controlled by a frequency controller, resulting in droplets having different radii on the horizontally oriented test surface placed on the stage. The experiments were performed at 6-7 V, 5-500 Hz (f), and a sample-dispenser spacing of $\approx$ 6 mm. Imaging was carried out at 7-100X magnification depending on the droplet size. The stage was illuminated by a LED source (AITECSYSTEM, TSPA22x8). The ambient temperature and relative humidity values were recorded using a handheld device (Omega HX93BD). For the purposes of visualizing dispensed microdroplet mobility, videos were captured at frame rates ranging from 5000 to 10000 fps.

The setup was used to print monodisperse microdroplets of water ($R \approx 9$ μm) onto a larger evaporating droplet ($R \gg 9$ μm) residing on the sample. The frequency of microdroplet deposition (f) was modulated to match the rate of evaporation, thereby attaining steady state with a fixed droplet size ($R \approx 100$ μm). At steady state, the rate of deposition of microdroplets was calculated

from the dispensing frequency and volume of individual microdroplets which was equal to the rate of evaporation. High speed videos (>5000 fps) were also taken to visually inspect the motion of the dispensed microdroplets as they approached the liquid-vapor interface of the larger evaporating droplet. Transient-based evaporation measurements on similar-sized droplets were also performed to benchmark the steady method. To conduct transient measurements, the large droplet was allowed to fully evaporate by turning off the flow of microdroplets and recording the total time of evaporation.

Supporting Information

Supporting Information is available from the Wiley Online Library or from the author.

Supporting Information includes thermal resistance analysis, four additional figures and nine videos showing cloaking dynamics on LISs.

Acknowledgements

The authors gratefully acknowledge funding support from the National Science Foundation under Award No. 1554249. The authors gratefully acknowledge funding support from the Office of Naval Research (ONR) under Grant No. N00014-16-1-2625. N.M. gratefully acknowledges funding support from the International Institute for Carbon Neutral Energy Research (WPI-I2CNER), sponsored by the Japanese Ministry of Education, Culture, Sports, Science and Technology. This work was also supported by the Khalifa University Competitive Internal Research Award (CIRA-2018-121) and the U.S. National Academy of Sciences Arab-American Frontiers Fellowship Award.

Received: ((will be filled in by the editorial staff))
Revised: ((will be filled in by the editorial staff))
Published online: ((will be filled in by the editorial staff))

References

[1] a) R. Kandasamy, X.-Q. Wang, A. S. Mujumdar, *Applied Thermal Engineering* **2008**, 28, 1047; b) M. Jaworski, *Applied Thermal Engineering* **2012**, 35, 212; c) J. Oh, P. Birbarah, T. Foulkes, S. L. Yin, M. Rentauskas, J. Neely, R. C. N. Pilawa-Podgurski, N. Miljkovic, *Applied Physics Letters* **2017**, 110, 123107.

[2] a) M. M. Farid, A. M. Khudhair, S. A. K. Razack, S. Al-Hallaj, *Energy Conversion and Management* **2004**, 45, 1597; b) H. Ghasemi, G. Ni, A. M. Marconnet, J. Loomis, S. Yerci, N. Miljkovic, G. Chen, *Nature Communications* **2014**, 5, 4449.

[3] a) T. J. Lu, *International Journal of Heat and Mass Transfer* **2000**, 43, 2245; b) R. Kandasamy, X.-Q. Wang, A. S. Mujumdar, *Applied Thermal Engineering* **2007**, 27, 2822; c) A. Pasupathy, R. Velraj, R. V. Seeniraj, *Renewable and Sustainable Energy Reviews* **2008**, 12, 39.

[4] F. Agyenim, N. Hewitt, P. Eames, M. Smyth, *Renewable and Sustainable Energy Reviews* **2010**, 14, 615.

[5] a) E. M. Sparrow, S. H. Lin, *Journal of Heat Transfer* **1964**, 86, 430; b) N. Miljkovic, E. N. Wang, *MRS Bulletin* **2013**, 38, 397; c) N. Miljkovic, R. Enright, Y. Nam, K. Lopez, N. Dou, J. Sack, E. N. Wang, *Nano Letters* **2013**, 13, 179.

[6] a) N. Zuber, *Trans. Am. Soc. Mech. Engrs.* **1958**, Medium: X; Size: Pages: 711; b) S. M. You, J. H. Kim, K. H. Kim, *Applied Physics Letters* **2003**, 83, 3374; c) R. Chen, M.-C. Lu, V. Srinivasan, Z. Wang, H. H. Cho, A. Majumdar, *Nano Letters* **2009**, 9, 548.

[7] a) C. H. B. PRIESTLEY, R. J. TAYLOR, *Monthly Weather Review* **1972**, 100, 81; b) S. Chandra, M. di Marzo, Y. M. Qiao, P. Tartarini, *Fire Safety Journal* **1996**, 27, 141; c) A. A. Günay, S. Sett, J. Oh, N. Miljkovic, *Langmuir* **2017**, 33, 12007.

[8] a) H. J. Cho, D. J. Preston, Y. Zhu, E. N. Wang, *Nature Reviews Materials* **2016**, 2, 16092; b) R. Enright, N. Miljkovic, J. L. Alvarado, K. Kim, J. W. Rose, *Nanoscale and Microscale Thermophysical Engineering* **2014**, 18, 223; c) D. Attinger, C. Frankiewicz, A. R. Betz, T. M. Schutzius, R. Ganguly, A. Das, C.-J. Kim, C. M. Megaridis, *MRS Energy & Sustainability* **2014**, 1.

[9] N. Miljkovic, D. J. Preston, R. Enright, E. N. Wang, *ACS Nano* **2013**, 7, 11043.

[10] M. Yamada, B. Shen, T. Imamura, S. Hidaka, M. Kohno, K. Takahashi, Y. Takata, *International Journal of Heat and Mass Transfer* **2017**, 115, 753.

[11] a) G. Azimi, R. Dhiman, H.-M. Kwon, A. T. Paxson, K. K. Varanasi, *Nature Materials* **2013**, 12, 315; b) J. B. Boreyko, C.-H. Chen, *Physical Review Letters* **2009**, 103, 184501.

[12] a) D. J. Preston, Z. Lu, Y. Song, Y. Zhao, K. L. Wilke, D. S. Antao, M. Louis, E. N. Wang, *Scientific Reports* **2018**, 8, 540; b) S. Sett, P. Sokalski, K. Boyina, L. Li, K. F. Rabbi, H. Auby, T. Foulkes, A. Mahvi, G. Barac, L. W. Bolton, N. Miljkovic, *Nano Letters* **2019**, 19, 5287.

[13] a) T.-S. Wong, S. H. Kang, S. K. Y. Tang, E. J. Smythe, B. D. Hatton, A. Grinthal, J. Aizenberg, *Nature* **2011**, 477, 443; b) S. Anand, A. T. Paxson, R. Dhiman, J. D. Smith, K. K. Varanasi, *ACS Nano* **2012**, 6, 10122; c) J. D. Smith, R. Dhiman, S. Anand, E. Reza-Garduno, R. E. Cohen, G. H. McKinley, K. K. Varanasi, *Soft Matter* **2013**, 9, 1772.

[14] D. J. Preston, Y. Song, Z. Lu, D. S. Antao, E. N. Wang, *ACS applied materials & interfaces* **2017**, 9, 42383.

[15] P. Kim, T.-S. Wong, J. Alvarenga, M. J. Kreder, W. E. Adorno-Martinez, J. Aizenberg, *ACS nano* **2012**, 6, 6569.

[16] A. K. Epstein, T.-S. Wong, R. A. Belisle, E. M. Boggs, J. Aizenberg, *Proceedings of the National Academy of Sciences* **2012**, 109, 13182.
[17] T.-S. Wong, S. H. Kang, S. K. Tang, E. J. Smythe, B. D. Hatton, A. Grinthal, J. Aizenberg, *Nature* **2011**, 477, 443.
[18] C. Howell, A. Grinthal, S. Sunny, M. Aizenberg, J. Aizenberg, *Advanced materials* **2018**, 30, 1802724.
[19] S. Sett, X. Yan, G. Barac, L. W. Bolton, N. Miljkovic, *ACS Applied Materials & Interfaces* **2017**, 9, 36400.
[20] a) J. Sun, V. V. Manepalli, P. B. Weisensee, *arXiv preprint arXiv:2003.02113* **2020**; b) J. Sun, P. B. Weisensee, *Soft Matter* **2019**, 15, 4808.
[21] G. Mistura, M. Pierno, *Advances in Physics: X* **2017**, 2, 591.
[22] A. Carlson, P. Kim, G. Amberg, H. A. Stone, *EPL (Europhysics Letters)* **2013**, 104, 34008.
[23] a) F. M. Fowkes, *Journal of colloid and interface science* **1968**, 28, 493; b) F. M. Etzler, *Reviews of Adhesion and Adhesives* **2013**, 1, 3.
[24] C. J. van Oss, *Colloids and Surfaces A: Physicochemical and Engineering Aspects* **1993**, 78, 1.
[25] Q. Ge, A. Raza, H. Li, S. Sett, N. Miljkovic, T. Zhang, *ACS Applied Materials & Interfaces* **2020**, DOI: 10.1021/acsami.9b22417.
[26] S. J. Gokhale, J. L. Plawsky, P. C. W. Jr., S. DasGupta, *Physics of Fluids* **2004**, 16, 1942.
[27] a) T. Josyula, Z. Wang, A. Askounis, D. Orejon, S. Harish, Y. Takata, P. S. Mahapatra, A. Pattamatta, *Physical Review E* **2018**, 98, 052804; b) X. Xu, J. Luo, *Applied Physics Letters* **2007**, 91, 124102; c) Z. Pan, S. Dash, J. A. Weibel, S. V. Garimella, *Langmuir* **2013**, 29, 15831.
[28] C. C. Miller, *Proceedings of the Royal Society of London. Series A, Containing Papers of a Mathematical and Physical Character* **1924**, 106, 724.
[29] X. Yan, L. Zhang, S. Sett, L. Feng, C. Zhao, Z. Huang, H. Vahabi, A. K. Kota, F. Chen, N. Miljkovic, *ACS Nano* **2019**, 13, 1309.
[30] S. Anand, K. Rykaczewski, S. B. Subramanyam, D. Beysens, K. K. Varanasi, *Soft matter* **2015**, 11, 69.
[31] V. Bergeron, D. Langevin, *Physical Review Letters* **1996**, 76, 3152.
[32] G. E. Cossali, A. Coghe, M. Marengo, *Experiments in Fluids* **1997**, 22, 463.
[33] J. B. Boreyko, G. Polizos, P. G. Datskos, S. A. Sarles, C. P. Collier, *Proceedings of the National Academy of Sciences* **2014**, 111, 7588.
[34] F. Schellenberger, J. Xie, N. Encinas, A. Hardy, M. Klapper, P. Papadopoulos, H.-J. Butt, D. Vollmer, *Soft Matter* **2015**, 11, 7617.
[35] G. K. Batchelor, *An introduction to fluid dynamics*, Cambridge University Press.
[36] D. J. Griffiths.
[37] V. P. Carey, *Liquid-vapor phase-change phenomena: an introduction to the thermophysics of vaporization and condensation processes in heat transfer equipment*, CRC Press, **2020**.
[38] D. Tam, V. von ARNIM, G. McKinley, A. Hosoi, *Journal of Fluid Mechanics* **2009**, 624, 101.
[39] Y. Yuan, T. R. Lee, in *Surface Science Techniques*, DOI: 10.1007/978-3-642-34243-1_1 (Eds: G. Bracco, B. Holst), Springer Berlin Heidelberg, Berlin, Heidelberg **2013**, p. 3.
[40] a) M. J. Kreder, D. Daniel, A. Tetreault, Z. Cao, B. Lemaire, J. V. Timonen, J. Aizenberg, *Physical Review X* **2018**, 8, 031053; b) J. S. Wexler, I. Jacobi, H. A. Stone, *Physical review letters* **2015**, 114, 168301.
[41] a) A. Marmur, M. Nosonovsky, F. Guittard, I. S. Bayer, S. Franssila, K.-Y. Law, P. A. Levkin, L. Jiang, K. K. Varanasi, A. Amirfazli, *Non-wettable surfaces: theory, preparation and*

applications, Royal Society of Chemistry, **2016**; b) H. Y. Erbil, *Surface Innovations* **2016**, 4, 214.

[42] M. J. Kreder, J. Alvarenga, P. Kim, J. Aizenberg, *Nature Reviews Materials* **2016**, 1, 1.

[43] S. B. Subramanyam, K. Rykaczewski, K. K. Varanasi, *Langmuir* **2013**, 29, 13414.

[44] D. Daniel, J. V. I. Timonen, R. Li, S. J. Velling, J. Aizenberg, *Nature Physics* **2017**, 13, 1020.

[45] a) N. Miljkovic, R. Enright, Y. Nam, K. Lopez, N. Dou, J. Sack, E. N. Wang, *Nano letters* **2012**, 13, 179; b) R. Enright, N. Miljkovic, N. Dou, Y. Nam, E. N. Wang, *Journal of Heat Transfer* **2013**, 135, 091304.

[46] a) K. S. Boyina, A. J. Mahvi, S. Chavan, D. Park, K. Kumar, M. Lira, Y. Yu, A. A. Gunay, X. Wang, N. Miljkovic, *International Journal of Heat and Mass Transfer* **2019**, 145, 118694; b) Y. Zhou, W. Yi-Zhi, Y. Yi-Fan, G. Mao-Gang, X. Xiao-Liang, *Chinese Physics B* **2012**, 21, 126801.

[47] H. Cha, J. M. Chun, J. Sotelo, N. Miljkovic, *ACS Nano* **2016**, 10, 8223.

Table 1. Relevant properties of lubricants and working fluids at 25°C.

	Liquid Density, ρ_l [kg m^{-3}]	**Vapor Pressure, P_v [kPa]**	**Liquid-Vapor Surface Tension, σ [mN m^{-1}]**	**Dynamic Viscosity, μ [mPa s]**	**Type of Oil**
Lubricant					
K1506	1880	5×10^{-8}	17	113	Fluorinated
K1525	1900	1.3×10^{-8}	19	496	Fluorinated
K16256	1920	4×10^{-15}	19	5216	Fluorinated
Fomblin Y25/6	1900	8×10^{-9}	22	524	Fluorinated
Carnation Oil	810	0.01	28	9.7	Mineral
BMIm	1430	N/A	34	64	Ionic liquid
SO-5	918	0.7	19	4.6	Silicone
SO-1000	971	0.7	21	971	Silicone
Working Fluid					
DI Water	997	2.33	72.7	0.89	NA
Ethanol	789	5.83	24.8	1.095	NA

Table 2. Lubricant – working fluid interfacial tension ($\boldsymbol{\sigma}$) and spreading coefficient ($\boldsymbol{S}$) calculated using Equation 1-2. A positive spreading coefficient ($\boldsymbol{S} > 0$) indicates cloaking of the droplet by the lubricant is energetically favored. Miscible indicates that the lubricant and working fluids are miscible.

Lubricant	Lubricant - Water Interfacial Tension, $\sigma_{l,w}$ [mN m^{-1}]	Water - Spreading Coefficient, S_w [mN m^{-1}]	Lubricant - Ethanol Interfacial Tension, $\sigma_{l,e}$ [mN m^{-1}]	Ethanol - Spreading Coefficient, S_e [mN m^{-1}]
K1506	51.2	4.5	2.6	1.8
K1525	51.0	2.7	2.6	-0.2
K16256	51.0	2.7	2.6	-0.2
Fomblin Y25/6	50.9	-0.2	2.7	-3.3
Carnation Oil	51.3	-6.6	3.5	-10.1
BMIm[a]	13	-4.8	N/A	Miscible
BMIm[b]	13	26	N/A	Miscible
SO-5	51.0	2.0	2.6	Miscible
SO-1000	50.9	0.6	2.7	Miscible

[a]Considering partial solubility of BMIm in water (γ_l = 42 mN m^{-1})[13b]

[b]Considering no solubility of BMIm in water (γ_l = 72.7 mN m^{-1})[25]

Table 3. Time scales relevant to cloaking of lubricants on water droplets residing on LISs where $t_{tot,m}$ and $t_{tot,n}$ are the times for the monolayer and nanolayer respectively to cloak the large evaporating droplet, $t_{s,m}$ and $t_{s,n}$ represent the times of reformation of the cloak layer for the monolayer and nanolayer, respectively, t_{dep} represents the depletion timescale of the cloaking layer, and t_{dis} is the time scale of droplet dispensing. The results indicate that for K16256 and SO-1000, the time scales are on the same order of magnitude; explaining the observed droplet mobility at the free interface.

Sample	Contact Angle [°]	R [μm]	Oh	$t_{tot,m}$ [ms]	$t_{tot,n}$ [ms]	$t_{s,m}$ [ms]	$t_{s,n}$ [ms]	t_{dep} [ms]	t_{dis} [ms]
K1506	122	190	1.45	1.97	1.32	0.09	0.06	0.19	12.5
K1525	117	210	5.7	5.2	5.72	0.22	0.25	0.82	12.5
K16256	115	150	70.51	7.31	42.95	0.44	2.58	8.81	12.5
F25/6	117	210	5.60	N/A	5.22	N/A	0.22	0.87	12.5
BMIm[a]	63	200	0.65	N/A	0.47	N/A	0.02	0.40	12.5
BMIm[b]	63	200	0.65	0.50	0.47	0.02	0.02	0.43	12.5
SO-5	105	210	0.07	1.03	0.53	0.04	0.02	0.12	16.7
SO-1000	100	210	14.77	14.27	10.03	0.61	0.43	1.61	16.7

[a]Considering partial solubility of BMIm in water (γ_l = 42 mN m^{-1})[13b]

[b]Considering no solubility of BMIm in water (γ_l = 72.7 mN m^{-1})[25]

Table 4. Calculated vs. observed radial group velocities of the cloaking copper oxide based samples. It is seen that there is a difference in the values caused by the movement of the oil layer around the water droplet. Negative value indicates movement against gravity.

LIS Sample Lubricant	Calculated Group Velocity, $v_{g,r}$ [cm s^{-1}]	Experimentally Measured Satellite Droplet Velocity v_{exp} [cm s^{-1}]
K1506	3.2	2.22 ± 0.1
K1525	2.9	-0.35 ± 0.1
K16256	2.5	1.26 ± 0.1
F25/6	2.9	0.54 ± 0.1
BMIm	2.7	1.52 ± 0.1
SO-5	1.4	0.03 ± 0.1
SO-1000	1.1	0.04 ± 0.1

Table 5. Apparent contact angles, predicted radial group velocity (Equation 19) and experimentally observed velocity of the formed satellite droplets on the interface for different LISs using both CuO and boehmite structured surfaces.

	F25/6		**K16256**		**SO-1000**	
	CuO	**AlO(OH)**	**CuO**	**AlO(OH)**	**CuO**	**AlO(OH)**
$\boldsymbol{\theta_{a,water}}$ **[°]**	117.0	107.8	115.3	104.2	100.4	93.8
$\boldsymbol{\theta_{r,water}}$ **[°]**	113.9	104.4	113.5	101.6	97.2	90.4
$\boldsymbol{\Delta\theta_{water}}$ **[°]**	3.1	3.4	1.8	2.6	3.2	3.4
$\boldsymbol{v_{g,r}}$ **[cm s^{-1}]**	2.91	0.85	2.46	0.59	1.11	0.06
$\boldsymbol{v_{exp}}$ **[cm s^{-1}]**	0.54	0.44	1.26	1.04	0.04	0.03

Table 6. Apparent advancing contact angle ($\boldsymbol{\theta_a}$), apparent receding contact angle ($\boldsymbol{\theta_r}$), and contact angle hysteresis ($\Delta\boldsymbol{\theta} = \boldsymbol{\theta_a} - \boldsymbol{\theta_r}$) of water droplets residing on LIS. All measurements were done on CuO-based LISs.

Sample	$\boldsymbol{\theta_a}$ [°]	$\boldsymbol{\theta_r}$ [°]	$\Delta\boldsymbol{\theta}$ [°]
K1506	121.7 ± 1.6	119.4 ± 2.9	2.3 ± 3.3
K1525	116.8 ± 2.1	113.7 ± 2.6	3.1 ± 3.3
K16256	115.3 ± 2.1	113.5 ± 2.6	1.8 ± 3.3
F25/6	117.0 ± 1.9	113.9 ± 2.8	3.1 ± 3.4
Carn	101.3 ± 4.5	97.2 ± 5.5	4.1 ± 7.1
BMIm	62.5 ± 1.9	60.2 ± 3.6	2.3 ± 4.1
SO-5	104.6 ± 2.5	100.8 ± 4.2	3.8 ± 4.9
SO-1000	100.4 ± 1.9	97.2 ± 5.5	3.2 ± 5.8
Si-HTMS	114.8 ± 1.8	101.3 ± 6.8	13.5 ± 7.0

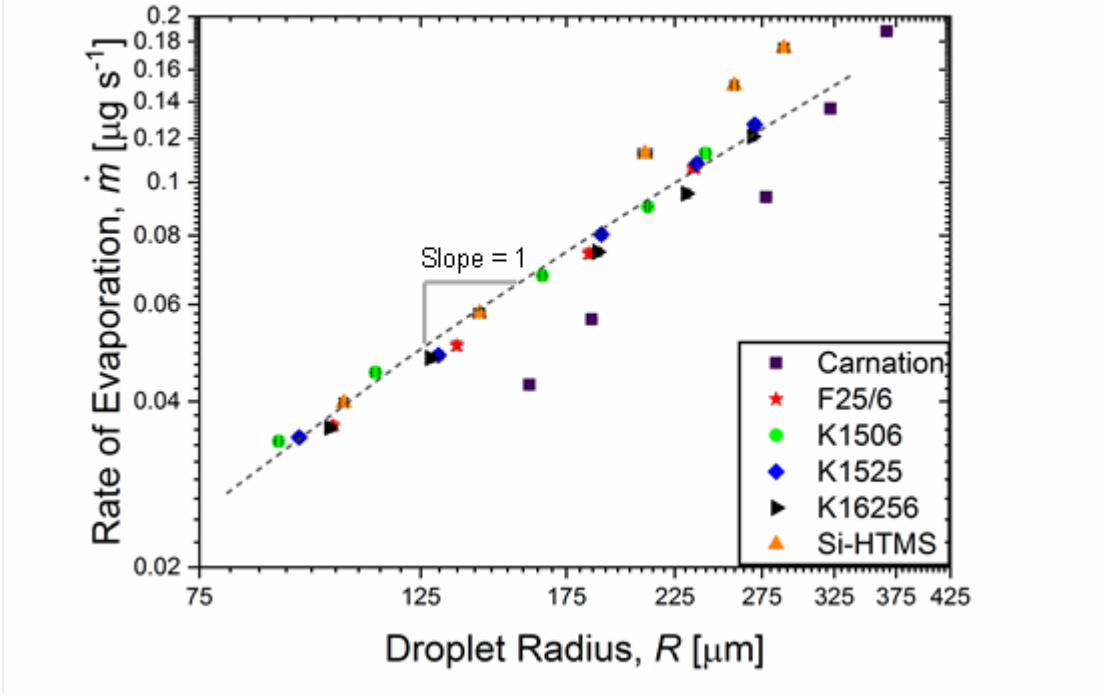

Figure 1. Water droplet rate of evaporation ($\dot{\boldsymbol{m}}$) as a function of droplet radius of curvature ($\boldsymbol{R}$) (see Table 6 for apparent contact angle data). The rate of evaporation scales linearly with the droplet radius of curvature since majority of evaporation occurs at the contact line for large evaporating droplets ($\boldsymbol{R} > \mathbf{100}\ \boldsymbol{\mu m}$)[7c]. Water droplets on LISs exhibited slightly lower $\dot{\boldsymbol{m}}$ due to cloaking. Experiments were performed at $\boldsymbol{T}_{\infty} = 25 \pm 0.5$°C, $\boldsymbol{\phi}$ = 50% ± 5%.

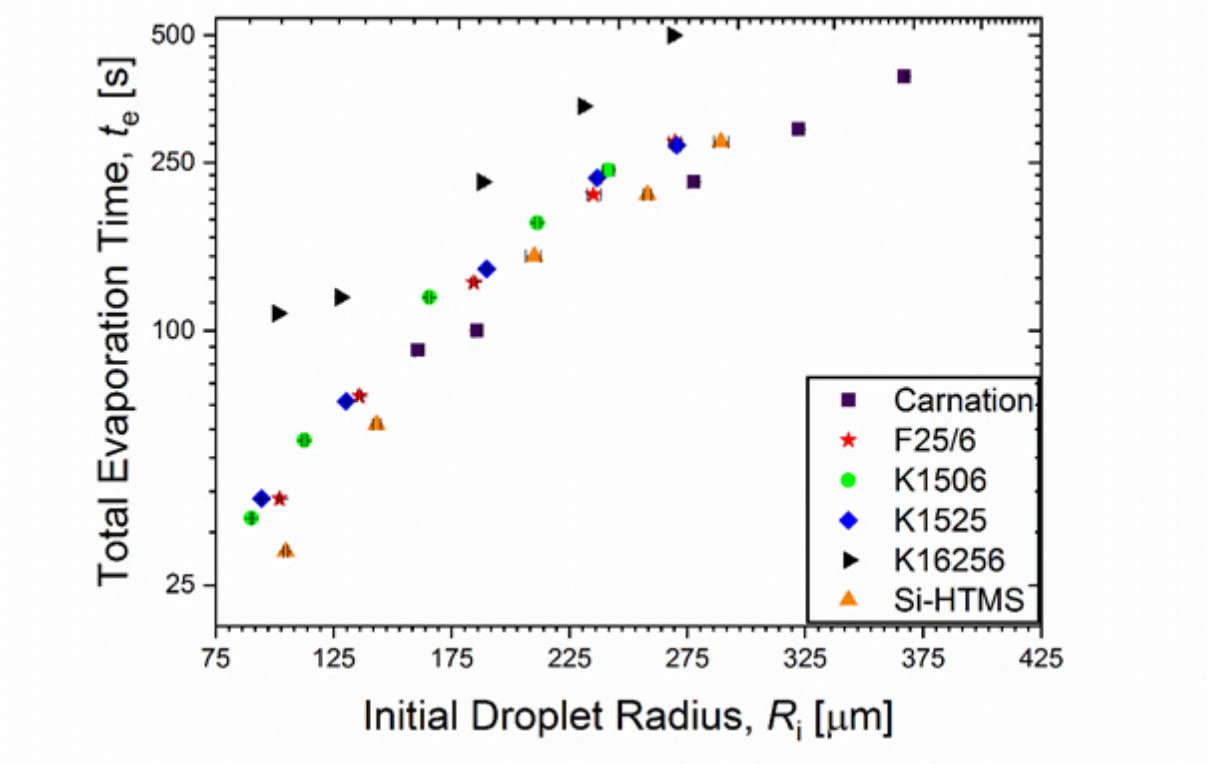

Figure 2. Total evaporation time as a function of the initial water droplet radius of curvature for the transient method experiments. The K16256 takes much longer times to evaporate due to the added layer of lubricant encapsulating the outer shell of the droplet. Experiments were performed at $T_\infty = 25 \pm 0.5$°C, ϕ = 50% ± 5%.

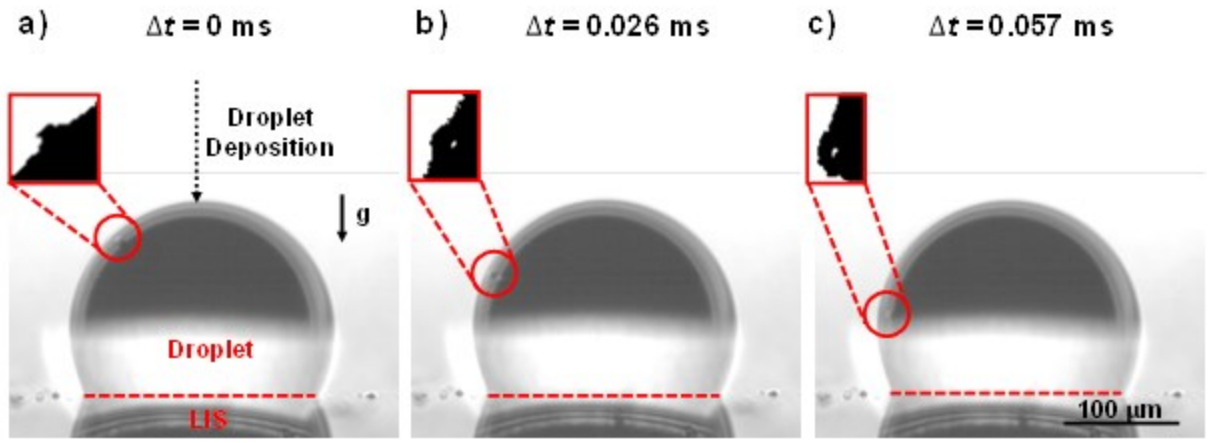

Figure 3. Time-lapse side-view images of a cloaked water droplet evaporating on a K16256 LIS when the flow of monodisperse droplets is turned on ($\boldsymbol{f}$ = 40 Hz). The movement of the incoming monodisperse microdroplets (red-circle) due to the presence of a mobile layer of cloaked lubricant can be observed directly. Tracking of the monodisperse droplets enabled the study of interfacial dynamics. Images inside the red-boxes represent black-white treated analysis to visualize the microdroplets. Experiments were performed at ambient conditions of $\boldsymbol{T}_{\infty} = 23.9 \pm 0.5$ ℃, $\boldsymbol{\phi}$ = 33.8% $\pm$ 1.7%. Image acquisition rate was 10,000 fps. See Video S3.

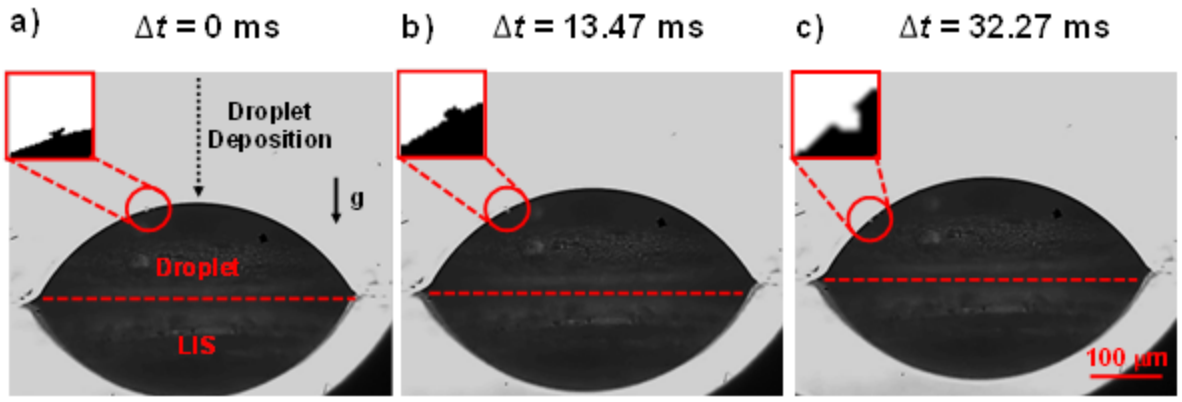

Figure 4. Time-lapse side-view images of a cloaked water droplet evaporating on a BMIm LIS when the flow of monodisperse droplets is f = 80 Hz. Movement of the incoming monodisperse microdroplets occurs (red circle) due to the presence of the mobile cloaking layer. Monodisperse droplets were observed to move inward (toward the center) for (c), altering the contrast of the inset image. Experiments were performed at ambient conditions of $T_\infty = 22.7 \pm 0.5$ °C, ϕ = 25.0% ± 1.3%. Image acquisition rate was 7,500 fps. See Video S4.

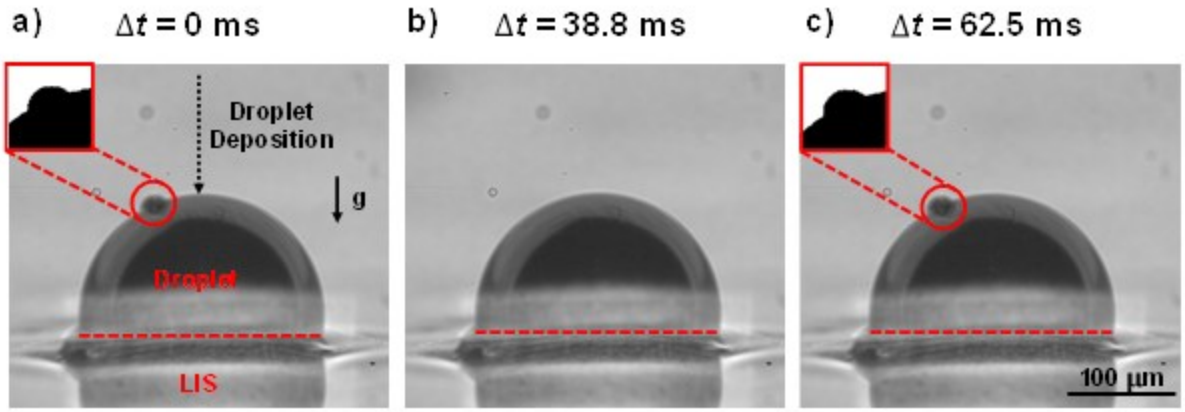

Figure 5. Time-lapse side-view images of a cloaked water droplet evaporating on a boehmite SO-1000 LIS when the flow of monodisperse droplets is f = 60 Hz. The movement of incoming microdroplets (red circle) due to the presence of a mobile layer of cloaked lubricant is observed. The satellite microdroplet impacts the evaporating droplet, and (a) moves on the interface, (b) coalesces with the evaporating droplet after sufficient time, and (c) the cycle restarts with the arrival of another monodisperse microdroplet. Experiments were performed at ambient conditions of $T_\infty = 23.1 \pm 0.5$°C, ϕ = 22.5% ± 1%. Image acquisition rate was 10,000 fps. See Video S5.

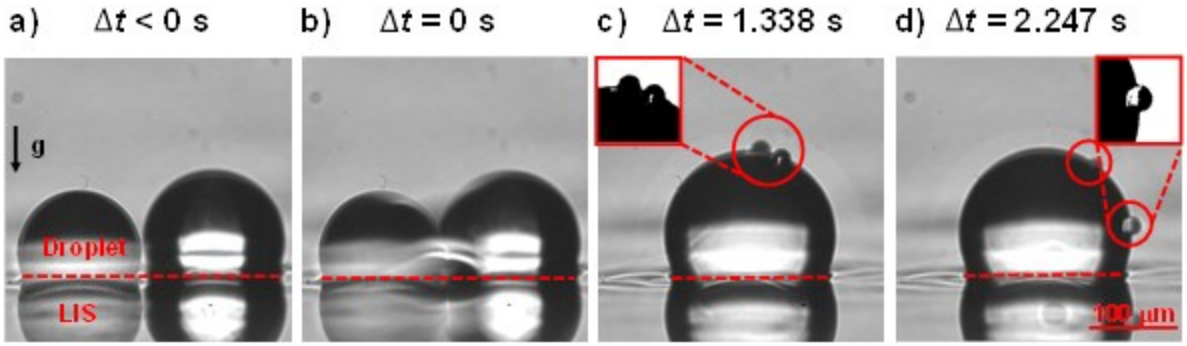

Figure 6. Side-view time-lapse images of two sessile water droplets evaporating on a CuO-based K1525 LIS when the flow of monodisperse droplets is $\boldsymbol{f}$ = 60 Hz. Images (a) before, (b) during, and (c-d) after coalescence (note that the focus is different due to slight difference in spatial locations of the droplets). Enhanced droplet mobility is observed in (c-d) due to capillary forces transferring lubricant to the droplet interface, increasing the effect of cloaking. Experiments were performed at ambient conditions of $\boldsymbol{T}_{\infty} = 23.1 \pm 0.5$ °C, $\boldsymbol{\phi}$ = 22.5% $\pm$ 1%. Time $\boldsymbol{t}$ = 0 represents the instant droplets coalesced. Image acquisition rate was 10,000 fps. See Video S7.

Cloaking phenomenon on Lubricant-Infused Surfaces (LISs) significantly alters phase change dynamics and decreases the overall lifetime of LISs. We show that droplet cloaking by the lubricant cannot be predicted purely by thermodynamic considerations. Rather, dynamics of coalescence, droplet formation and surface interactions also need to be considered.

Keyword

Keywords: Evaporation, Lubricant, LIS, Cloaking, Coalescence

Cloaking Dynamics on Lubricant-Infused Surfaces